

Hyperbolic Active Learning for Semantic Segmentation under Domain Shift

Luca Franco^{1,3*} Paolo Mandica^{1,3*} Konstantinos Kallidromitis¹
 Devin Guillory² Yu-Teng Li² Fabio Galasso³

¹AI Lab, Panasonic R&D Company of America

²UC Berkeley ³Sapienza University of Rome

Abstract

For the task of semantic segmentation (SS) under domain shift, active learning (AL) acquisition strategies based on image regions and pseudo labels are state-of-the-art (SoA). The presence of diverse pseudo-labels within a region identifies pixels between different classes, which is a labeling efficient active learning data acquisition strategy. However, by design, pseudo-label variations are limited to only select the contours of classes, limiting the final AL performance.

We approach AL for SS in the Poincaré hyperbolic ball model for the first time and leverage the variations of the radii of pixel embeddings within regions as a novel data acquisition strategy. This stems from a novel geometric property of a hyperbolic space trained without enforced hierarchies, which we experimentally prove. Namely, classes are mapped into compact hyperbolic areas with a comparable intra-class radii variance, as the model places classes of increasing explainable difficulty at denser hyperbolic areas, i.e. closer to the Poincaré ball edge. The variation of pixel embedding radii identifies well the class contours, but they also select a few intra-class peculiar details, which boosts the final performance.

Our proposed HALO (Hyperbolic Active Learning Optimization) surpasses the supervised learning performance for the first time in AL for SS under domain shift, by only using a small portion of labels (i.e., 1%). The extensive experimental analysis is based on two established benchmarks, i.e. GTAV → Cityscapes and SYNTHIA → Cityscapes, where we set a new SoA. The code will be released.

1 Introduction

Dense prediction tasks such as semantic segmentation (SS) require pixel-wise annotations which can be costly and time inefficient [10]. Previous methods [31, 43, 44, 53, 58] have addressed this labeling challenge through the use of domain adaptation, capitalizing on large source datasets for pre-training and domain-adapting with few target annotations [3]. Most recently, active domain adaptation (ADA) selects only a small, fixed number of target pixels to manually annotate [31]. State-of-the-art (SoA) ADA leverages regions and pseudo labels as the active learning (AL) data acquisition strategy [44, 56, 58]. Combined with prediction entropy, the most effective such strategy is region impurity [58], which selects regions with diverse pseudo-labels, more likely to be class contours. However, the implicit focus of pseudo labels and region impurity to class contours limits the final performance of AL. We argue and experimentally show that a few details within the (complex) objects are beneficial, too.

We propose Hyperbolic Active Learning Optimization (HALO), the first hyperbolic neural network for AL, and a novel geometric interpretation of the hyperbolic radius. The SoA hyperbolic SS model [2]

*Equal contribution

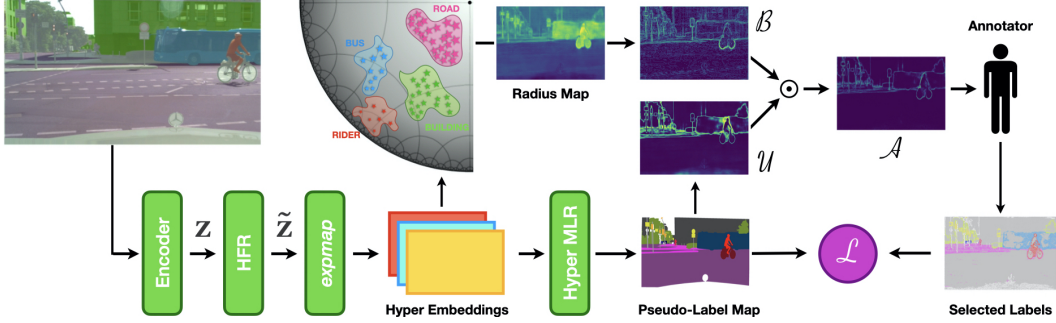


Figure 1: Overview of HALO. Pixels are encoded into the feature map Z , reweighted by the HFR module, and mapped onto the hyperbolic Poincaré disk. The hyperbolic radius variations of the pixel embeddings define the new hyperbolic boundaries \mathcal{B} . Pixel embeddings also define a pseudo-label map via hyperbolic multinomial logistic regression (MLR), from which their uncertainty \mathcal{U} is estimated via entropy. Finally, the data acquisition map \mathcal{A} is used to query new pixel labels.

trains with class hierarchies, which they define. As a result, their hyperbolic radius represents the parent-to-child hierarchical relation in the Poincaré ball. We adopt [2], but we find that hierarchies do not emerge naturally when not enforcing them at training. E.g., in HALO *road* and *building* classes are closer to the center of the ball, while *person* and *rider* have larger radii. This class arrangement can also not be explained by considering the hyperbolic radius as a proxy to uncertainty, as it emerges with metric learning hyperbolic objectives [11, 12], because *road* and *building* are effectively less uncertain classes. So neither hierarchies nor uncertainty explains the learned radii in the case of the hierarchy-free hyperbolic multinomial logistic regression pixel classification of HALO.

We identify a novel interpretation of the hyperbolic radius. Let us consider the HALO pipeline in Fig. 1 and the circular sector, depicting the Poincaré ball, whereby pixels from different classes are mapped. HALO learns a manifold whereby classes occupy compact areas and their radius variance is mostly constant, cf. Sec. 4. The value of the radius correlates with the inherent complexity of the class and with the scarcity of labels for it. E.g. *road* (magenta) has lower radius than *rider* (red), because *road* has less diversity of appearance and many more labelled pixels. HALO achieves class compactness by mapping more complex and less known classes closer to the edge, where the Poincaré ball has exponentially larger volumes available. Effectively, in the radius map of Fig. 1, class pixels take nearly constant values. The radius variations define our proposed *hyperbolic boundaries*, which are the core of our proposed AL data acquisition strategy, i.e. sample new labels according to their strength (cf. 5). Hyperbolic boundaries mostly occur at the contour of classes, in line with RIPU [58], but they also sample a few details within classes, which boosts performance (see results in Sec. 6).

Upon extensive benchmarking on established datasets for SS via ADA, GTAV \rightarrow Cityscapes, SYNTHIA \rightarrow Cityscapes, HALO sets a new SoA and it surpasses fully-supervised learning, for the first time. Our framework includes a novel technique for stabilizing hyperbolic training, which we dub *Hyperbolic Feature Reweighting* (HFR), cf. Sec. 5. Key contributions are summarized as follows:

1. we identify a novel geometric interpretation of the hyperbolic radius, representing inherent complexity of a class, in average, and how much it is known about it;
2. we introduce novel hyperbolic boundaries, defining a new AL data acquisition score;
3. we conduct extensive analysis and tests for validating the idea and the algorithm.

2 Related Works

Hyperbolic Representation Learning (HRL) Hyperbolic geometry has been extensively used to capture embeddings of tree-like structures [4, 30] with low distortion [39, 40]. Since the seminal work of Ganea *et al.* [16] on Hyperbolic Neural Networks (HNN), approaches have successfully combined hyperbolic geometry with model architectures ranging from convolutional [42] to attention-based [18], including graph neural networks [5, 24] and, most recently, vision transformers [11]. There are two leading interpretations of the hyperbolic radius in hyperbolic space: as a measure of the prediction uncertainty [6, 11, 12] or as the hierarchical parent-to-child relation [2, 11, 30, 50, 51].

Our work builds on the SoA hyperbolic semantic segmentation method of [2], which enforces hierarchical labels and training objectives. However, when training hierarchy-free for ADA, as we do, the hierarchical interpretation does not apply; nor the uncertainty viewpoint is applicable. To the best of our knowledge, we are the first to propose a third interpretation for the HNNs connecting the hyperbolic space density to the semantic class recognition difficulty.

Active Learning (AL) The number of annotations required for dense tasks such as semantic segmentation can be costly and time-consuming. Active learning balances the labelling efforts and performance, selecting most informative pixels in successive learning rounds. Strategies for active learning are based on uncertainty sampling [15, 54, 55], diversity sampling [1, 22, 41, 57] or a combination of both [48, 58, 59]. For the case of AL in semantic segmentation, EqualAL [17] incorporates the self-supervisory signal of self-consistency to mitigate overfitting of scenarios with limited labeled training data. Labor [44] selects the most representative pixels within the generation of an inconsistency mask. PixelPick [43] prioritizes the identification of specific pixels or regions over labeling the entire image. [29] explores the effect of data distribution, semi-supervised learning, and labeling budgets.

We are the first to leverage hyperbolic neural networks for AL of semantic segmentation. Our novel data acquisition score leverages the hyperbolic radius variations as a proxy to the most informative for inter- and intra-class pixel selection.

Active Domain Adaptation (ADA) Domain Adaptation (DA) involves learning from a source data distribution and transferring that knowledge to a target dataset with a different distribution. Recent advancements in DA for semantic segmentation have utilized unsupervised (UDA) [20, 25, 26, 28, 53, 60] and semi-supervised (SSDA) [13, 21, 38, 46] learning techniques. However, challenges such as noise and label bias still pose limitations on the performance of DA methods.

Active Domain Adaptation (ADA) aims to reduce the disparity between source and target domains by actively selecting informative data points from the target domain [14, 44, 47, 49], which are subsequently labeled by human annotators. In semantic segmentation, Ning *et al.* [31] propose a multi-anchor strategy to mitigate the distortion between the source and target distributions. Prabhu *et al.* [34] propose a clustering approach that utilizes uncertainty and diversity in data distributions. Our work is motivated by the recent study of Xie *et al.* [58], which shows the advantages of region-based selection, in terms of region impurity and entropy scores, compared to pixel-based methods. We introduce a novel acquisition score that builds upon a region-based strategy, but instead of relying solely on predicted pseudo-labels, we leverage data distributions in the hyperbolic manifold.

3 Background

We provide preliminaries on two techniques that HALO builds on: Hyperbolic Image Segmentation [2] and RIPU [58].

3.1 Hyperbolic Image Segmentation

Atigh *et al.* [2] has been the first to demonstrate a performance of hyperbolic SS on par with Euclidean. They proceed by mapping pixel embeddings onto a hyperbolic space, where they classify by hyperbolic multinomial logistic regression.

Hyperbolic Neural Networks We operate in the Poincaré ball hyperbolic space. We define the pair $(\mathbb{D}_c^N, g^{\mathbb{D}_c})$ where $\mathbb{D}_c^N = \{x \in \mathbb{R}^N : c\|x\| < 1\}$ is the manifold and $g_x^{\mathbb{D}_c} = (\lambda_x^c)^2 g^{\mathbb{E}}$ is the associated Riemannian metric, $-c$ is the curvature, $\lambda_x^c = \frac{2}{1-c\|x\|^2}$ is the conformal factor and $g^{\mathbb{E}} = \mathbb{I}^N$ is the Euclidean metric tensor. Hyperbolic neural networks first extract a feature vector v in Euclidean space, which is subsequently projected into the Poincaré ball through an exponential map:

$$\exp_x^c(v) = x \oplus_c \left(\frac{v}{\sqrt{c}\|v\|} \tanh \left(\sqrt{c} \frac{\lambda_x^c \|v\|}{2} \right) \right) \quad (1)$$

where h, w are hyperbolic vectors, x is the anchor and \oplus_c is the Möbius hyperbolic addition, defined as follows:

$$h \oplus_c w = \frac{(1 + 2c\langle h, w \rangle + c\|w\|^2)v + (1 - c\|h\|^2)w}{1 + 2c\langle h, w \rangle + c^2\|h\|^2\|w\|^2} \quad (2)$$

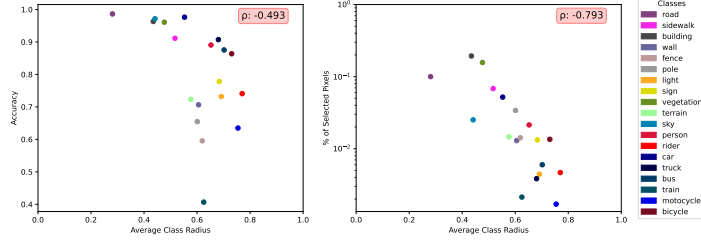


Figure 2: (a) Plot of average per-class radii of pixel embeddings Vs. class accuracies; (b) Plot of average per-class radii of pixel embeddings Vs. the percentage of per-class-selected target pixels (percentages refer to what selected with an AL budget of 5%).

Hyperbolic Multinomial Logistic Regression (MLR) Following [16], we project each feature z_i onto the Poincaré ball $h_i = \exp_x^c(z_i) \in \mathbb{D}_c^N$ and classify with a number of hyperplanes for each class y , also known as "gyroplanes":

$$H_y^c = \{h_i \in \mathbb{D}_c^N, \langle -p_y \oplus_c h_i, w_y \rangle\}, \quad (3)$$

where, p_y represents the gyroplane offset, and w_y represents the orientation for class y . The distance between a Poincaré ball embedding h_i and the gyroplane H_y^c is given by:

$$d(h_i, H_y^c) = \frac{1}{\sqrt{c}} \sinh^{-1} \left(\frac{2\sqrt{c} \langle -p_y \oplus_c h_i, w_y \rangle}{(1 - c\| -p_y \oplus_c h_i\|^2)\|w_y\|} \right), \quad (4)$$

Based on this distance, we define the likelihood as $p(\hat{y}_i = y|h_i) \propto \exp(\zeta_y(h_i))$ and the logit for the y class as $\zeta_y(h_i) = \lambda_{p_y}^c \|w_y\| d(h_i, H_y^c)$.

3.2 RIPU

RIPU [58] is the SoA on active domain adaptation (ADA) for SS. The task aims to transfer knowledge from a source labeled dataset $\mathcal{S} = (X_s, Y_s)$ to a target unlabeled dataset $\mathcal{T} = (X_t, Y_t)$, where X represents an image and Y the corresponding annotation map. Y_s is given, Y_t is initially the empty set \emptyset . Following the AL protocol, RIPU selects pixels in stages according to a data acquisition strategy. Specifically, they use pixel- and region-based pixel statistics, the prediction uncertainty and region impurity, respectively.

Region Impurity and Prediction Uncertainty Using the target image X_t as input, the model generates a target prediction $\mathbf{P}_t^{(i,j,c)}$ at each pixel i, j for the class $c \in [0, C]$. The uncertainty \mathcal{U} for k -neighbor squared non-overlapping regions is the average predictive entropy of pixels $\mathcal{H}^{(i,j)}$:

$$\mathcal{H}^{(i,j)} = - \sum_{c=1}^C \mathbf{P}_t^{(i,j,c)} \log \mathbf{P}_t^{(i,j,c)} \quad (5)$$

The region impurity \mathcal{P} is computed from the pseudo-labels within the regions, estimated via $\arg \max_c \mathbf{P}_t^{(i,j,c)}$, by the entropy of the ratio of label occurrences. The final acquisition score is defined as $\mathcal{A} = \mathcal{P} \odot \mathcal{U}$, where \odot is the element-wise matrix multiplication. The regions with the highest score are selected for labeling in the active round.

Since it is based on pseudo-labels, the region impurity score focuses on inter-class contours, which limits the data acquisition strategy from capturing intra-class details, also meaningful for recognition.

4 Novel Geometric Interpretation of the Hyperbolic Space

We propose to use the variation of the hyperbolic radius of the pixel embeddings as a novel region-based data acquisition strategy. This is motivated by a novel geometric interpretation of the hyperbolic radius, which we support with experimental evidence in this section.

Setup We assume to have pre-trained the hyperbolic image segmenter of [2] on GTAV [35] and to have domain-adapted it to Cityscape [10] with 5 rounds of AL, each adding 1% of the target labels.

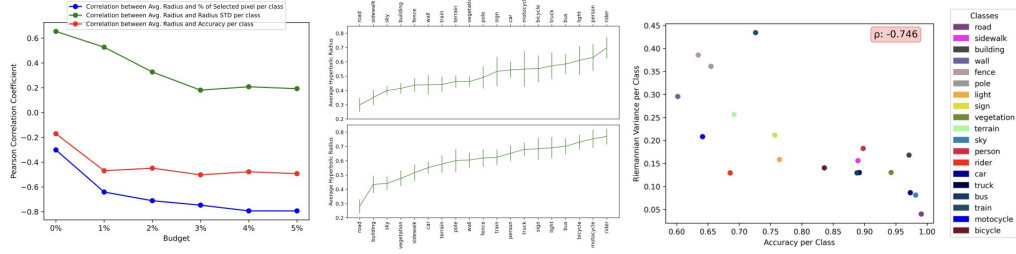


Figure 3: (a) AL evolution of the correlations between the average class radius Vs. the following, per class: (blue) % of selected pixels, (red) SS accuracy and (green) standard deviation of the radius; (b) Plots of class average radii and standard deviations, (top) before ADA and (bottom) after ADA – classes are sorted by increasing radii; (c) Plot of class accuracies Vs. their Riemannian variance. See Sec. 4 for details.

We assume to have followed the HALO pipeline of Fig. 1, which we detail in Sec. 5. The rest of this section considers the radii of the hyperbolic pixel embeddings, for which statistics are computed on the Cityscape [10] validation set.

What does the hyperbolic radius represent? Fig. 2a illustrates the correlation between the per-class average radius and the relative class SS accuracy. They correlate negatively with a significant $\rho = -0.493$. So classes with larger hyperbolic radii have lower performance and are likely more difficult to recognize, more complex. E.g. *road* has large accuracy and small radius, *rider* has lower accuracy and larger radius.

Fig. 2b additionally shows the correlation between the average class radius and the percentage of selected pixel labels for the class (the percentage refers to having acquired 5% of the target labels). This correlation is also significant ($\rho = -0.793$), so classes with larger hyperbolic radii such as *rider* have been seen the least in training.

We conclude that *the hyperbolic radius indicates the difficulty in recognizing a class*, as a consequence of the class complexity and its label scarcity.

How does learning the hyperbolic manifold of the pixels embeddings proceed? Fig. 3a illustrates the evolution, during the active learning rounds, of the correlations between the per-class average radius and three quantities: the standard deviation (STD) of the radius (green), the classification accuracy (red), and the percentage of pixels selected for the considered class (blue). During training, both the correlations of the radius Vs. accuracy and the radius Vs. %-selected-pixels grow in module, confirming that the model progressively learns hyperbolic radii, indicative of the recognition difficulty of the class, based on the inherent complexity and label scarcity.

By contrast, the correlation radius Vs. STD drops. Insights are provided by the plots in Fig. 3b, where the average class radii and their STD are depicted, having sorted classes by their radii. Going from before-ADA statistics in the top plot to after-ADA statistics in the bottom one, the model learns to map the classes, so the STDs of classes are smaller and approximately constant.

We summarize this so: *the model progressively learns to map more difficult classes at larger radii, while keeping all classes equally compact around their average radius*.

Figure 3c complements the findings by plotting the class accuracies Vs. the Riemannian variance (see Appendix) of radii for each class. The latter generalizes the Euclidean variance, taking into consideration the increasing Poincaré ball density at larger radii. The correlation of accuracies Vs. Riemannian variance is significant ($\rho = -0.746$). So more difficult classes such as *pole* which have lower accuracy, also have the larger Riemannian variance, so the largest effective volume available. We conclude that *the model accomplishes class compactness on the hyperbolic space by placing more complex classes at larger radii*, where the space is denser and there is more volume to model them.

Comparing interpretations of the hyperbolic radius It emerges from our analysis that hyperbolic radii are approximately constant within classes and that larger radii are assigned to classes that are more difficult to recognize, for their inherent complexity and their label scarcity.

Earlier work has explained the hyperbolic radius in terms of uncertainty or hierarchies. Techniques from the former [6, 11, 12] consider that the larger hyperbolic radii indicate more certain and unambiguous samples. This is typical of hyperbolic metric learning-based approaches, whereby the larger radius results in an exponentially larger matching penalty due to the employed Poincaré

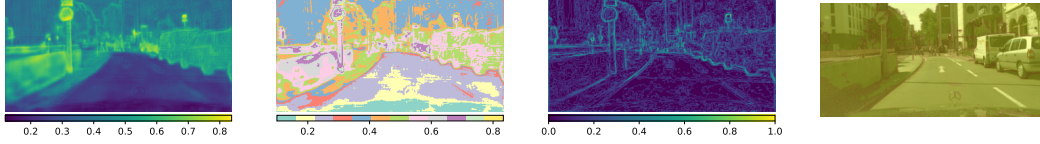


Figure 4: (a) Radius map depicting the hyperbolic radii of pixel embeddings; (b) Quantized radius map, according to discrete intervals of radius variations; (c) Proposed hyperbolic boundaries, computed within k -neighbor squared regions on each pixel; (d) Pixels (in red) that have been selected for data acquisition. See Sec. 4 for details.

distance (see Appendix). We argue that this yields a self-normalizing learning objective, effectively making the radius proportional to the errors, as those techniques show.

Methods in favor of a hierarchical explanation [2, 11, 30, 50, 51] consider hierarchical datasets, labeling, and classification objective functions. Hierarchies naturally align with the growing volume in the Poincaré ball, so children nodes from different parents are mapped further from each other than from their parents. Learning under hierarchical constraints results in leaf classes closer to the ball edge, and moving between them passes via their parents at lower hyperbolic radii.

Our hyperbolic SS model is derived from [2] but it differs in the geometric meaning of the hyperbolic radii of pixel embeddings. We believe that our novel interpretation emerges due to the use of the hyperbolic multinomial logistic regression objective without the enforced label hierarchies.

From hyperbolic geometry to active learning data acquisition Fig. 4a illustrates the hyperbolic *radius map*, i.e. the radii of the hyperbolic pixel embeddings in the image. Note that the radii are approximately constant within the classes, as expected, and that radius variations mark the class boundaries.

Fig. 4b depicts the quantized radius map, i.e. the variability range of the radius is assigned distinct labels, shown in the picture as distinct colors. Using the quantized radius map considers radius variations, independently of the value differences.

Fig. 4c shows the proposed hyperbolic boundaries, computed from the number and distribution of the quantized radius map values within k -neighbor squared regions (see Sec. 5 for the details). The more quantized radius values within the region, the more likely there is a class contour, and the larger the region score. Note however that hyperbolic boundaries also emphasize, though to a lower extent, a few details within the classes, instrumental to better recognize them.

Finally, Fig. 4d illustrates the pixels selected for data acquisition, according to hyperbolic boundaries.

5 Hyperbolic Active Learning Optimization (HALO)

We review the HALO pipeline, we delve into the novel hyperbolic boundaries and AL acquisition strategy, and we present our proposition for fixing the instability of the hyperbolic framework.

HALO pipeline Let us consider Fig. 1. Following the SoA hyperbolic semantic segmenter [2], images are processed into pixel embeddings via an encoder and an expmap, which projects onto the Poincaré ball. The hyperbolic multinomial logistic regression (Hyper MLR) serves the training, after the target labels are selected by the data acquisition strategy, and the estimation of pseudo-labels. On parallel branches, the pixel embeddings are used to estimate the proposed hyperbolic boundaries \mathcal{B} (cf. Sec. 4 and Fig. 4), and the pseudo-labels are used to estimate pixel uncertainties \mathcal{U} , as in RIPU [58] (cf. Sec.3). New labels are then selected according to the data acquisition score $\mathcal{A} = \mathcal{B} \odot \mathcal{U}$, and added to the training annotations. Following the ADA protocol [58], training labels include all source (Y_s) and selected target annotations (initially empty $Y_t = \emptyset$), added in rounds, according to a budget, upon querying an annotator. The architecture is end-to-end trained, backpropagating the estimates ($\hat{\cdot}$) from the per-pixel loss $\mathcal{L}(\{\hat{Y}_s, \hat{Y}_t\}, \{Y_s, Y_t\})$.

Hyperbolic Boundaries Hyperbolic boundaries are computed from the hyperbolic pixel embedding radii. Following literature [2], we assume a hyperbolic curvature of $c = 1$, so the hyperbolic embeddings of pixels $h_{ij} = \text{expmap}(z_{ij})$ have radii $r_{ij} \in [0, 1]$. We quantize the radius range uniformly into K discrete values I_k with $k = 1, \dots, K$. This yields the quantized radius map R^q :

$$r_{ij}^q = k \quad \text{if } r_{ij} \in I_k, \quad (6)$$

Table 1: Comparison of mIoU results for different methods on the **GTAV** \rightarrow **Cityscapes** task. Methods marked with \sharp are based on DeepLab-v3+ [8], whereas all the others use DeepLab-v2 [7].

| Method | road | sidew. | build. | wall | fence | pole | light | sign | veg. | terr. | sky | pers. | rider | car | truck | bus | train | motor | bike | mIoU |
|---------------------------------------|-------------|-------------|-------------|-------------|-------------|-------------|-------------|-------------|-------------|-------------|-------------|-------------|-------------|-------------|-------------|-------------|-------------|-------------|-------------|-------------|
| Eucl. Source Only | 75.8 | 16.8 | 77.2 | 12.5 | 21.0 | 25.5 | 30.1 | 20.1 | 81.3 | 24.6 | 70.3 | 53.8 | 26.4 | 49.9 | 17.2 | 25.9 | 6.5 | 25.3 | 36.0 | 36.6 |
| Hyper. Source Only | 62.4 | 18.7 | 66.8 | 17.4 | 13.8 | 29.2 | 30.4 | 7.4 | 83.2 | 23.8 | 78.2 | 56.1 | 30.3 | 70.6 | 25.0 | 17.8 | 0.3 | 27.6 | 27.0 | 36.1 |
| Hyper. Source Only \sharp | 71.7 | 22.6 | 76.6 | 26.6 | 14.8 | 31.5 | 32.6 | 11.9 | 83.8 | 22.8 | 79.9 | 59.7 | 27.3 | 62.2 | 29.3 | 35.8 | 10.2 | 26.6 | 14.8 | 38.9 |
| CBST [64] | 91.8 | 53.5 | 80.5 | 32.7 | 21.0 | 34.0 | 28.9 | 20.4 | 83.9 | 34.2 | 80.9 | 53.1 | 24.0 | 82.7 | 30.3 | 35.9 | 16.0 | 25.9 | 42.8 | 45.9 |
| MRKLD [65] | 91.0 | 55.4 | 80.0 | 33.7 | 21.4 | 37.3 | 32.9 | 24.5 | 85.0 | 34.1 | 80.8 | 57.7 | 24.6 | 84.1 | 27.8 | 30.1 | 26.9 | 26.0 | 42.3 | 47.1 |
| Seg-Uncertainty [63] | 90.4 | 31.2 | 85.1 | 36.9 | 25.6 | 37.5 | 48.8 | 48.5 | 85.3 | 34.8 | 81.1 | 64.4 | 36.8 | 86.3 | 34.9 | 52.2 | 1.7 | 29.0 | 44.6 | 50.3 |
| TPLD [45] | 94.2 | 60.5 | 82.8 | 36.6 | 16.6 | 39.3 | 29.0 | 25.5 | 85.6 | 44.9 | 84.4 | 60.6 | 27.4 | 84.1 | 37.0 | 47.0 | 31.2 | 36.1 | 50.3 | 51.2 |
| DPL-Dual [9] | 92.8 | 54.4 | 86.2 | 41.6 | 32.7 | 36.4 | 49.0 | 34.0 | 85.8 | 41.3 | 86.0 | 63.2 | 34.2 | 87.2 | 39.3 | 44.5 | 18.7 | 42.6 | 43.1 | 53.3 |
| ProDA [62] | 87.8 | 56.0 | 79.7 | 46.3 | 44.8 | 45.6 | 53.5 | 53.5 | 88.6 | 45.2 | 82.1 | 70.7 | 39.2 | 88.8 | 45.5 | 59.4 | 1.0 | 48.9 | 56.4 | 57.5 |
| WeakDA (point) [33] | 94.0 | 62.7 | 86.3 | 36.5 | 32.8 | 38.4 | 44.9 | 51.0 | 86.1 | 43.4 | 87.7 | 66.4 | 36.5 | 87.9 | 44.1 | 58.8 | 23.2 | 35.6 | 55.9 | 56.4 |
| LabOR (2.2%) [44] | 96.6 | 77.0 | 89.6 | 47.8 | 50.7 | 48.0 | 56.6 | 63.5 | 89.5 | 57.8 | 91.6 | 72.0 | 47.3 | 91.7 | 62.1 | 61.9 | 48.9 | 47.9 | 65.3 | 66.6 |
| RIPU (2.2%) [58] | 96.5 | 74.1 | 89.7 | 53.1 | 51.0 | 43.8 | 53.4 | 62.2 | 90.0 | 57.6 | 92.6 | 73.0 | 53.0 | 92.8 | 73.8 | 78.5 | 62.0 | 55.6 | 70.0 | 69.6 |
| Ours (2.2%) | 97.4 | 79.8 | 90.5 | 53.6 | 51.4 | 49.9 | 57.7 | 67.6 | 90.5 | 59.7 | 93.0 | 74.4 | 54.6 | 92.3 | 61.9 | 76.2 | 62.9 | 56.4 | 69.5 | 70.6 |
| AADA (5%) \sharp [49] | 92.2 | 59.9 | 87.3 | 36.4 | 45.7 | 46.1 | 50.6 | 59.5 | 88.3 | 44.0 | 90.2 | 69.7 | 38.2 | 90.0 | 55.3 | 45.1 | 32.0 | 32.6 | 62.9 | 59.3 |
| MADA (5%) \sharp [31] | 95.1 | 69.8 | 88.5 | 43.3 | 48.7 | 45.7 | 53.3 | 59.2 | 89.1 | 46.7 | 91.5 | 73.9 | 50.1 | 91.2 | 60.6 | 56.9 | 48.4 | 51.6 | 68.7 | 64.9 |
| D ² ADA (5%) \sharp [56] | 97.0 | 77.8 | 90.0 | 46.0 | 55.0 | 52.7 | 58.7 | 65.8 | 90.4 | 58.9 | 92.1 | 75.7 | 54.4 | 92.3 | 69.0 | 78.0 | 68.5 | 59.1 | 72.3 | 71.3 |
| RIPU (5%) \sharp [58] | 97.0 | 77.3 | 90.4 | 54.6 | 53.2 | 47.7 | 55.9 | 64.1 | 90.2 | 59.2 | 93.2 | 75.0 | 54.8 | 92.7 | 73.0 | 79.7 | 68.9 | 55.5 | 70.3 | 71.2 |
| Ours (5%)\sharp | 97.7 | 81.5 | 91.3 | 53.5 | 56.4 | 62.7 | 71.9 | 91.3 | 59.4 | 94.3 | 77.9 | 58.0 | 93.9 | 77.9 | 77.9 | 83.9 | 70.6 | 58.9 | 72.5 | 74.1 |
| Eucl. Fully Supervised | 96.8 | 77.5 | 90.0 | 53.5 | 51.5 | 47.6 | 55.6 | 62.9 | 90.2 | 58.2 | 92.3 | 73.7 | 52.3 | 92.4 | 74.3 | 77.1 | 64.5 | 52.4 | 70.1 | 70.2 |
| Hyper. Fully Supervised | 97.3 | 79.0 | 89.8 | 50.3 | 51.8 | 43.9 | 52.0 | 61.8 | 89.8 | 58.0 | 92.6 | 71.3 | 50.5 | 91.8 | 65.6 | 78.3 | 64.9 | 52.4 | 67.7 | 68.8 |
| Eucl. Fully Supervised \sharp | 97.4 | 77.9 | 91.1 | 54.9 | 53.7 | 51.9 | 57.9 | 64.7 | 91.1 | 57.8 | 93.2 | 74.7 | 54.8 | 93.6 | 76.4 | 79.3 | 67.8 | 55.6 | 71.3 | 71.9 |
| Hyper. Fully Supervised \sharp | 97.6 | 81.2 | 90.7 | 49.9 | 53.2 | 53.5 | 58.0 | 67.2 | 91.0 | 59.1 | 93.9 | 74.2 | 52.6 | 93.1 | 76.4 | 81.0 | 67.0 | 55.0 | 70.8 | 71.9 |

We propose an entropic formulation of the radius quantized variations within the regions, to consider the number and distribution of discrete intervals, rather than the actual radius value. We define the region around the pixel (i, j) as the neighborhood $\mathcal{N}_\ell(i, j) = \{(u, v) : |u - i| < \ell, |v - j| < \ell\}$, where ℓ is the radius of the region. So we define the hyperbolic boundary score $\mathcal{B}^{(i,j)}$ as follows:

$$\mathcal{B}^{(i,j)} = - \sum_{k=1}^K \frac{\mathcal{N}_\ell^k(i, j)}{|\mathcal{N}_\ell(i, j)|} \log \frac{\mathcal{N}_\ell^k(i, j)}{|\mathcal{N}_\ell(i, j)|} \quad (7)$$

where $\mathcal{N}_\ell^k(i, j) = \sum_{(u,v) \in \mathcal{N}_\ell(i,j)} \mathbb{1}_{r_{uv}^q=k}$ and $|\cdot|$ represents the cardinality of the set. $\mathcal{B}^{(i,j)}$ depends on the number of quantized values and their distribution, normalized on the region size.

Acquisition Score We formulate the acquisition score of each region as the element-wise multiplication of the hyperbolic boundaries \mathcal{B} of Eq. 7 and the uncertainties \mathcal{U} , estimated as the average region entropies of Eq. 5, i.e. $\mathcal{A} = \mathcal{B} \odot \mathcal{U}$.

This score serves as a surrogate indicator for the classification difficulty of each pixel. \mathcal{A} determines which pixels are presented to the human annotator for labeling, to augment the target label set Y_t .

Hyperbolic Feature Reweighting During training, HNN can be susceptible to instability issues due to the inherent topology of the hyperbolic manifold. Specifically, when embeddings are close to the border, vanishing gradients can occur, hindering the learning process. Several solutions have been proposed to address this problem, such as feature clipping [19], curriculum learning [12], and suitable weight initialization [52]. However, these approaches often yield sub-optimal or comparable performances when compared to the Euclidean counterpart. We introduce the *Hyperbolic Feature Reweighting (HFR)* module, designed to enhance training stability by reweighting features, prior to their projection onto the Poincaré ball. Given a feature map Z , we compute the weights as $L = \text{HRF}(Z) \in \mathbb{D}^{\tilde{H} \times \tilde{W}}$ and use them to rescale each entry of the normalized feature map, yielding $\tilde{Z} = \frac{Z}{|Z|} \odot L$, where $|Z| = \sum_{k=1}^{\tilde{H}\tilde{W}} z_{ij}$ and \odot denotes the element-wise multiplication.

6 Results

In this section, we describe the benchmarks and training protocols; we perform a comparative evaluation against the SoA (Sec. 6.1); and we conduct ablation studies on the components, setups and hyper-parameters of HALO (Sec. 6.2).

Datasets The model has been pre-trained using synthetic cityscapes images from the GTAV [35] and SYNTHIA [36] datasets. The **GTAV** dataset comprises of 24,966 high-resolution frames that are densely labeled and divided into 19 classes that are fully compatible with the Cityscapes [10] dataset. The **SYNTHIA** dataset contains a selection of 9,000 images with a resolution of 1280×760 and 16 classes. For ADA training and evaluation we consider the real-world urban street scenes from the **Cityscapes** as target dataset. The dataset comprises 2,975 training samples and 500 validation samples, with a resolution of 2048×1024 and is split into 19 classes.

Table 2: Comparison of mIoU results for different methods on the SYNTHIA \rightarrow Cityscapes task. Methods marked with \sharp are based on DeepLab-v3+ [8], whereas all the others use DeepLab-v2 [7].

| Method | road | sidew. | build. | wall* | fence* | pole* | light | sign | veg. | sky | pers. | rider | car | bus | motor | bike | mIoU | mIoU* |
|---------------------------------------|-------------|-------------|-------------|-------------|-------------|-------------|-------------|-------------|-------------|-------------|-------------|-------------|-------------|-------------|-------------|-------------|-------------|-------------|
| Eucl. Source Only | 64.3 | 21.3 | 73.1 | 2.4 | 1.1 | 31.4 | 7.0 | 27.7 | 63.1 | 67.6 | 42.2 | 19.9 | 73.1 | 15.3 | 10.5 | 38.9 | 34.9 | 40.3 |
| Hyper. Source Only | 36.4 | 21.1 | 56.4 | 13.3 | 0.1 | 24.8 | 0.0 | 9.5 | 78.8 | 70.4 | 54.2 | 8.6 | 77.9 | 35.8 | 11.7 | 27.3 | 32.9 | 37.5 |
| Hyper. Source Only \sharp | 60.5 | 27.4 | 75.2 | 13.3 | 0.3 | 31.4 | 0.0 | 23.2 | 79.3 | 68.1 | 57.8 | 18.7 | 61.3 | 27.3 | 10.3 | 23.5 | 36.1 | 41.0 |
| CBST [64] | 68.0 | 29.9 | 76.3 | 10.8 | 1.4 | 33.9 | 22.8 | 29.5 | 77.6 | 78.3 | 60.6 | 28.3 | 81.6 | 23.5 | 18.8 | 39.8 | 42.6 | 48.9 |
| MRKLD [65] | 67.7 | 32.2 | 73.9 | 10.7 | 1.6 | 37.4 | 22.2 | 31.2 | 80.8 | 80.5 | 60.8 | 29.1 | 82.8 | 25.0 | 19.4 | 45.3 | 43.8 | 50.1 |
| DPL-Dual [9] | 87.5 | 45.7 | 82.8 | 13.3 | 0.6 | 33.2 | 22.0 | 20.1 | 83.1 | 86.0 | 56.6 | 21.9 | 83.1 | 40.3 | 29.8 | 45.7 | 47.0 | 54.2 |
| TPLD [45] | 80.9 | 44.3 | 82.2 | 19.9 | 0.3 | 40.6 | 20.5 | 30.1 | 77.2 | 80.9 | 60.6 | 25.5 | 84.8 | 41.1 | 24.7 | 43.7 | 47.3 | 53.5 |
| Seg-Uncertainty [63] | 87.6 | 41.9 | 83.1 | 14.7 | 1.7 | 36.2 | 31.3 | 19.9 | 81.6 | 80.6 | 63.0 | 21.8 | 86.2 | 40.7 | 23.6 | 53.1 | 47.9 | 54.9 |
| ProDA [62] | 87.8 | 45.7 | 84.6 | 37.1 | 0.6 | 44.0 | 54.6 | 37.0 | 88.1 | 84.4 | 74.2 | 24.3 | 88.2 | 51.1 | 40.5 | 45.6 | 55.5 | 62.0 |
| WeakDA (point) [33] | 94.9 | 63.2 | 85.0 | 27.3 | 24.2 | 34.9 | 37.3 | 50.8 | 84.4 | 88.2 | 60.6 | 36.3 | 86.4 | 43.2 | 36.5 | 61.3 | 57.2 | 63.7 |
| RIPU (2.2%) [58] | 96.8 | 76.6 | 89.6 | 45.0 | 47.7 | 45.0 | 53.0 | 62.5 | 90.6 | 92.7 | 73.0 | 52.9 | 93.1 | 80.5 | 52.4 | 70.1 | 70.1 | 75.7 |
| Ours (2.2%) | 97.6 | 81.8 | 90.5 | 49.0 | 51.5 | 48.8 | 57.1 | 67.1 | 91.4 | 93.5 | 74.8 | 52.7 | 93.6 | 80.4 | 54.3 | 71.4 | 72.2 | 77.4 |
| AADA (5%) \sharp [49] | 91.3 | 57.6 | 86.9 | 37.6 | 48.3 | 45.0 | 50.4 | 58.5 | 88.2 | 90.3 | 69.4 | 37.9 | 89.9 | 44.5 | 32.8 | 62.5 | 61.9 | 66.2 |
| MADA (5%) \sharp [31] | 96.5 | 74.6 | 88.8 | 45.9 | 43.8 | 46.7 | 52.4 | 60.5 | 89.7 | 92.2 | 74.1 | 51.2 | 90.9 | 60.3 | 52.4 | 69.4 | 68.1 | 73.3 |
| D ² ADA (5%) \sharp [56] | 96.7 | 76.8 | 90.3 | 48.7 | 51.1 | 54.2 | 58.3 | 68.0 | 90.4 | 93.4 | 77.4 | 56.4 | 92.5 | 77.5 | 58.9 | 73.3 | 72.7 | 77.7 |
| RIPU (5%) \sharp [58] | 97.0 | 78.9 | 89.9 | 47.2 | 50.7 | 48.5 | 55.2 | 63.9 | 91.1 | 93.0 | 74.4 | 54.1 | 92.9 | 79.9 | 55.3 | 71.0 | 71.4 | 76.7 |
| Ours (5%)\sharp | 97.7 | 82.6 | 91.4 | 51.0 | 48.7 | 58.8 | 63.9 | 72.5 | 92.2 | 94.1 | 77.9 | 55.5 | 94.6 | 85.1 | 58.9 | 72.9 | 74.9 | 79.9 |
| Eucl. Fully Supervised | 96.7 | 77.8 | 90.2 | 40.1 | 49.8 | 52.2 | 58.5 | 67.6 | 91.7 | 93.8 | 74.9 | 52.0 | 92.6 | 70.5 | 50.6 | 70.2 | 70.6 | 75.9 |
| Hyper. Fully Supervised | 97.6 | 81.9 | 90.2 | 52.0 | 49.6 | 45.5 | 51.7 | 65.0 | 90.9 | 93.0 | 73.1 | 50.3 | 92.6 | 80.7 | 50.8 | 69.2 | 70.9 | 75.9 |
| Eucl. Fully Supervised \sharp | 97.5 | 81.4 | 90.9 | 48.5 | 51.3 | 53.6 | 59.4 | 68.1 | 91.7 | 93.4 | 75.6 | 51.9 | 93.2 | 75.6 | 52.0 | 71.2 | 72.2 | 77.1 |
| Hyper. Fully Supervised \sharp | 97.7 | 82.2 | 90.3 | 53.0 | 48.8 | 51.7 | 56.0 | 66.1 | 91.4 | 94.2 | 75.0 | 51.5 | 93.4 | 82.1 | 52.8 | 70.2 | 72.3 | 77.1 |

Training protocols The models undergo a source-only pre-training on either GTAV or SYNTHIA datasets. To compare and evaluate the performance with other methods, two ADA protocols are used: source-free and source+target. In the source-free protocol, only the Cityscapes dataset is used, whereas in the source+target protocol, both source and target datasets are utilized. In both protocols, our region-based pixel selection method is used to select pixels to be labeled in five evenly spaced rounds during training, with either 2.2% or 5% of total pixels selected. Fully-supervised models are trained for comparison purposes alongside the active learning protocol.

Evaluation metrics To assess the effectiveness of the models, the mean Intersection-over-Union (mIoU) metric is computed on the Cityscapes validation set. The mIoU is reported separately for GTAV-Cityscapes and SYNTHIA-Cityscapes experiments. For GTAV-Cityscapes, the mIoU is calculated on the shared 19 classes, whereas for SYNTHIA-Cityscapes, two mIoU values are reported, one on the 13 common classes (mIoU*) and another on the 16 common classes (mIoU).

Implementation details For all experiments, the model is trained on 4 Tesla V100 GPUs using PyTorch [32] and PyTorch Lightning with an effective batch-size of 8 samples (2 per GPU). The DeepLab-v3+ architecture is used with an Imagenet pre-trained ResNet-101 as the backbone.

RiemannianSGD optimizer with momentum of 0.9 and weight decay of 5×10^{-4} is used for all the trainings. The base learning rates for the encoder and decode head are 1×10^{-3} and 1×10^{-2} respectively, and they are decayed with a "polynomial" schedule with power 0.5. The models are pre-trained for 15K iterations and adapted for an additional 15K on the target set. As per RIPU [58], the source images are resized to 1280×720 , while the target images are resized to 1280×640 .

6.1 Comparison with the state-of-the-art

In Table 1, we present the results of our method and the most recent active learning approaches on the Cityscapes dataset after pre-training on GTAV and actively adapting with the source+target protocol. HALO outperforms the current state-of-the-art approaches (RIPU [58], D²ADA [56]), using both 2.2% (+1% mIoU) and 5% (+2.9% mIoU) of labeled pixels, reaching 70.6% and 74.1%, respectively. Additionally, our method is the first to surpass the fully-supervised baseline (71.9%), even by a significant margin (+2.2%). HALO achieves state-of-the-art also in the SYNTHIA \rightarrow Cityscapes case (cf. Table 2), where it improves by +2.1% and +3.5% using 2.2% and 5% of labels, reaching performances of 72.2% and 74.9%, respectively. Moreover, HALO is able to surpass the current best [58] by +3.3% in the source-free scenario, achieving performances close to the source+target when using DeepLab-v3+ and 5% budget (74.1% vs. 73.5%), as shown in Table 3.

6.2 Ablation Study

The extensive conducted ablation studies are gathered into Table 4 and discussed next.

Hyperbolic vs. Euclidean network In Table 1 and 2, the hyperbolic source-only pre-training, evaluated on the target set, achieves comparable performance to the Euclidean counterpart. However,

Table 3: HALO performance on the **source-free protocol** in comparison with previous UDA and ADA approaches.

| Method | Budget | mIoU |
|-------------------------|--------|-------------|
| URMA [37] | - | 45.1 |
| LD [61] | - | 45.5 |
| SFDA [23] | - | 53.4 |
| RIPU [58] | 2.2% | 67.1 |
| Ours | 2.2% | 70.4 |
| Ours[#] | 5% | 73.3 |

Table 4: Results of our ablation study conducted with the Hyperbolic DeepLab-v3+ as backbone, on the source+target protocol with 5% of labels. We analyze the impact on performance of various selection criteria and region sizes.

| Ablative version | Region Size | mIoU |
|--|--------------------------------|-------------|
| (a) Hyper Boundaries only | 5×5 | 63.4 |
| (b) Impurity only | 5×5 | 56.6 |
| (c) Entropy only | 5×5 | 63.2 |
| (d) Impurity + Entropy | 5×5 | 73.0 |
| (e) Hyper Boundaries + Entropy (HALO) | 5×5 | 74.1 |
| (f) Hyper Boundaries + Entropy | 3×3 | 73.8 |
| (g) Hyper Boundaries + Entropy | 7×7 | 73.7 |

in the ADA protocol, using RIPU’s acquisition strategy with an Hyperbolic model (method (d) in Table 4), we surpass RIPU (Euclidean, in Table 1) by +1.8% (73% Vs. 71.2%). This highlights the effectiveness of incorporating a hyperbolic network in enhancing the model’s performance.

Selection criteria HALO in Table 4 demonstrates an improvement of 1.1% compared to method (d). Particularly, without the incorporation of entropy, the performance gap widens significantly, reaching 6.8% (methods (a) Vs. (b)). These findings highlight the effectiveness of Hyperbolic Boundaries as a robust acquisition function, showcasing its superior performance over Impurity, both independently and in conjunction with entropy.

Region size Increasing the region size for the computation of Hyperbolic Boundaries improves performance up to a threshold (5×5), but beyond that, there is diminishing returns (methods (e), (f), and (g) in Table 4).

Labeling budget We experiment with different labeling budgets, observing performance improvements as the number of labeled pixels increases. However, beyond a threshold of 5%, adding more labeled pixels leads to diminishing returns due to data redundancy. Detailed results can be found in Figure 5.

Hyperbolic Feature Reweighting (HFR) HFR improves training stability and enhances performance in the Hyperbolic model. Although the mIoU improvement is modest (+1.2%), the main advantage is the training robustness, as the Hyperbolic model otherwise struggles to converge. HFR does not benefit the Euclidean model and instead negatively impacts its performance.

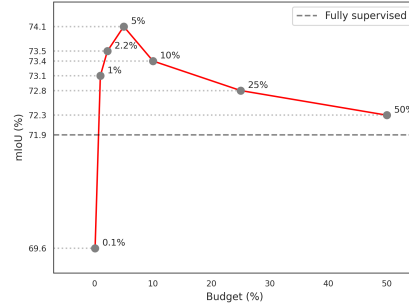


Figure 5: Performance on GTAV → Cityscapes with different budgets

7 Conclusions

We have introduced the first hyperbolic neural network technique for active learning, which we have extensively validated as the novel SoA on semantic segmentation under domain shift. We have identified a novel geometric interpretation of the hyperbolic radius, distinct from the established hyperbolic uncertainty and hyperbolic hierarchy, and we have supported the finding with experimental evidence. The novel concept of hyperbolic radius and its successful use as data acquisition strategy in AL are a step forward in understanding hyperbolic neural networks.

References

- [1] J. T. Ash, C. Zhang, A. Krishnamurthy, J. Langford, and A. Agarwal. Deep batch active learning by diverse, uncertain gradient lower bounds. *arXiv preprint arXiv:1906.03671*, 2019.
- [2] M. Atigh, J. Schoep, E. Acar, N. V. Noord, and P. Mettes. Hyperbolic image segmentation. In *2022 IEEE/CVF Conference on Computer Vision and Pattern Recognition (CVPR)*, pages 4443–4452, Los

Alamitos, CA, USA, jun 2022. IEEE Computer Society.

- [3] S. Ben-David, J. Blitzer, K. Crammer, A. Kulesza, F. Pereira, and J. Vaughan. A theory of learning from different domains. *Machine Learning*, 79:151–175, 2010.
- [4] I. Chami, A. Gu, V. Chatziafratis, and C. Ré. From trees to continuous embeddings and back: Hyperbolic hierarchical clustering. *Advances in Neural Information Processing Systems*, 33:15065–15076, 2020.
- [5] I. Chami, Z. Ying, C. Ré, and J. Leskovec. Hyperbolic graph convolutional neural networks. *Advances in neural information processing systems*, 32, 2019.
- [6] B. Chen, W. Peng, X. Cao, and J. Rönning. Hyperbolic uncertainty aware semantic segmentation. *arXiv preprint arXiv:2203.08881*, 2022.
- [7] L.-C. Chen, G. Papandreou, I. Kokkinos, K. Murphy, and A. L. Yuille. Deeplab: Semantic image segmentation with deep convolutional nets, atrous convolution, and fully connected crfs. *IEEE Transactions on Pattern Analysis and Machine Intelligence*, 40(4):834–848, Apr 2018.
- [8] L.-C. Chen, Y. Zhu, G. Papandreou, F. Schroff, and H. Adam. Encoder-decoder with atrous separable convolution for semantic image segmentation. In V. Ferrari, M. Hebert, C. Sminchisescu, and Y. Weiss, editors, *Computer Vision – ECCV 2018*, pages 833–851, Cham, 2018. Springer International Publishing.
- [9] Y. Cheng, F. Wei, J. Bao, D. Chen, F. Wen, and W. Zhang. Dual path learning for domain adaptation of semantic segmentation. In *Proceedings of the IEEE/CVF International Conference on Computer Vision*, pages 9082–9091, 2021.
- [10] M. Cordts, M. Omran, S. Ramos, T. Rehfeld, M. Enzweiler, R. Benenson, U. Franke, S. Roth, and B. Schiele. The cityscapes dataset for semantic urban scene understanding. *CoRR*, abs/1604.01685, 2016.
- [11] A. Ermolov, L. Mirvakhabova, V. Khrulkov, N. Sebe, and I. Oseledets. Hyperbolic vision transformers: Combining improvements in metric learning. In *Proceedings of the IEEE/CVF Conference on Computer Vision and Pattern Recognition*, pages 7409–7419, 2022.
- [12] L. Franco, P. Mandica, B. Munjal, and F. Galasso. Hyperbolic self-paced learning for self-supervised skeleton-based action representations. In *The Eleventh International Conference on Learning Representations*, 2023.
- [13] G. French, M. Mackiewicz, and M. Fisher. Self-ensembling for visual domain adaptation. *arXiv preprint arXiv:1706.05208*, 2017.
- [14] B. Fu, Z. Cao, J. Wang, and M. Long. Transferable query selection for active domain adaptation. In *Proceedings of the IEEE/CVF Conference on Computer Vision and Pattern Recognition*, pages 7272–7281, 2021.
- [15] Y. Gal, R. Islam, and Z. Ghahramani. Deep bayesian active learning with image data. In *International conference on machine learning*, pages 1183–1192. PMLR, 2017.
- [16] O. Ganea, G. Bécigneul, and T. Hofmann. Hyperbolic neural networks. *Advances in neural information processing systems*, 31, 2018.
- [17] S. A. Golestaneh and K. M. Kitani. Importance of self-consistency in active learning for semantic segmentation. *BMVC*, 2020.
- [18] C. Gulcehre, M. Denil, M. Malinowski, A. Razavi, R. Pascanu, K. M. Hermann, P. Battaglia, V. Bapst, D. Raposo, A. Santoro, et al. Hyperbolic attention networks. *arXiv preprint arXiv:1805.09786*, 2018.
- [19] Y. Guo, X. Wang, Y. Chen, and S. X. Yu. Clipped hyperbolic classifiers are super-hyperbolic classifiers. In *2022 IEEE/CVF Conference on Computer Vision and Pattern Recognition (CVPR)*, pages 1–10, Los Alamitos, CA, USA, jun 2022. IEEE Computer Society.
- [20] J. Hoffman, E. Tzeng, T. Park, J.-Y. Zhu, P. Isola, K. Saenko, A. Efros, and T. Darrell. Cycada: Cycle-consistent adversarial domain adaptation. In *International conference on machine learning*, pages 1989–1998. Pmlr, 2018.
- [21] P. Jiang, A. Wu, Y. Han, Y. Shao, M. Qi, and B. Li. Bidirectional adversarial training for semi-supervised domain adaptation. In *IJCAI*, pages 934–940, 2020.
- [22] A. Kirsch, J. van Amersfoort, and Y. Gal. Batchbald: Efficient and diverse batch acquisition for deep bayesian active learning, 2019.

- [23] J. N. Kundu, A. Kulkarni, A. Singh, V. Jampani, and R. V. Babu. Generalize then adapt: Source-free domain adaptive semantic segmentation. In *Proceedings of the IEEE/CVF International Conference on Computer Vision (ICCV)*, pages 7046–7056, October 2021.
- [24] Q. Liu, M. Nickel, and D. Kiela. Hyperbolic graph neural networks. *Advances in neural information processing systems*, 32, 2019.
- [25] Y. Liu, W. Zhang, and J. Wang. Source-free domain adaptation for semantic segmentation. In *Proceedings of the IEEE/CVF Conference on Computer Vision and Pattern Recognition*, pages 1215–1224, 2021.
- [26] Z. Liu, Z. Miao, X. Pan, X. Zhan, D. Lin, S. X. Yu, and B. Gong. Open compound domain adaptation. In *Proceedings of the IEEE/CVF Conference on Computer Vision and Pattern Recognition*, pages 12406–12415, 2020.
- [27] A. Lou, I. Katsman, Q. Jiang, S. Belongie, S.-N. Lim, and C. D. Sa. Differentiating through the fréchet mean, 2021.
- [28] K. Mei, C. Zhu, J. Zou, and S. Zhang. Instance adaptive self-training for unsupervised domain adaptation. In *Computer Vision–ECCV 2020: 16th European Conference, Glasgow, UK, August 23–28, 2020, Proceedings, Part XXVI 16*, pages 415–430. Springer, 2020.
- [29] S. Mittal, J. Niemeijer, J. P. Schäfer, and T. Brox. Best practices in active learning for semantic segmentation, 2023.
- [30] M. Nickel and D. Kiela. Poincaré embeddings for learning hierarchical representations, 2017.
- [31] M. Ning, D. Lu, D. Wei, C. Bian, C. Yuan, S. Yu, K. Ma, and Y. Zheng. Multi-anchor active domain adaptation for semantic segmentation. In *Proceedings of the IEEE/CVF International Conference on Computer Vision*, pages 9112–9122, 2021.
- [32] A. Paszke, S. Gross, F. Massa, A. Lerer, J. Bradbury, G. Chanan, T. Killeen, Z. Lin, N. Gimelshein, L. Antiga, A. Desmaison, A. Kopf, E. Yang, Z. DeVito, M. Raison, A. Tejani, S. Chilamkurthy, B. Steiner, L. Fang, J. Bai, and S. Chintala. Pytorch: An imperative style, high-performance deep learning library. In *Advances in Neural Information Processing Systems 32*, pages 8024–8035. Curran Associates, Inc., 2019.
- [33] S. Paul, Y.-H. Tsai, S. Schuler, A. K. Roy-Chowdhury, and M. Chandraker. Domain adaptive semantic segmentation using weak labels, 2020.
- [34] V. Prabhu, A. Chandrasekaran, K. Saenko, and J. Hoffman. Active domain adaptation via clustering uncertainty-weighted embeddings. In *Proceedings of the IEEE/CVF International Conference on Computer Vision*, pages 8505–8514, 2021.
- [35] S. R. Richter, V. Vineet, S. Roth, and V. Koltun. Playing for data: Ground truth from computer games. In B. Leibe, J. Matas, N. Sebe, and M. Welling, editors, *European Conference on Computer Vision (ECCV)*, volume 9906 of *LNCS*, pages 102–118. Springer International Publishing, 2016.
- [36] G. Ros, L. Sellart, J. Materzynska, D. Vazquez, and A. M. Lopez. The synthia dataset: A large collection of synthetic images for semantic segmentation of urban scenes. In *The IEEE Conference on Computer Vision and Pattern Recognition (CVPR)*, June 2016.
- [37] P. T. S and F. Fleuret. Uncertainty reduction for model adaptation in semantic segmentation. In *2021 IEEE/CVF Conference on Computer Vision and Pattern Recognition (CVPR)*, pages 9608–9618, 2021.
- [38] K. Saito, D. Kim, S. Sclaroff, T. Darrell, and K. Saenko. Semi-supervised domain adaptation via minimax entropy. In *Proceedings of the IEEE/CVF International Conference on Computer Vision (ICCV)*, October 2019.
- [39] F. Sala, C. De Sa, A. Gu, and C. Ré. Representation tradeoffs for hyperbolic embeddings. In *International conference on machine learning*, pages 4460–4469. PMLR, 2018.
- [40] R. Sarkar. Low distortion delaunay embedding of trees in hyperbolic plane. In *Graph Drawing: 19th International Symposium, GD 2011, Eindhoven, The Netherlands, September 21-23, 2011, Revised Selected Papers 19*, pages 355–366. Springer, 2012.
- [41] O. Sener and S. Savarese. Active learning for convolutional neural networks: A core-set approach. *arXiv preprint arXiv:1708.00489*, 2017.
- [42] R. Shimizu, Y. Mukuta, and T. Harada. Hyperbolic neural networks++. *arXiv preprint arXiv:2006.08210*, 2020.

- [43] G. Shin, W. Xie, and S. Albanie. All you need are a few pixels: semantic segmentation with pixelpick. In *Proceedings of the IEEE/CVF International Conference on Computer Vision*, pages 1687–1697, 2021.
- [44] I. Shin, D.-J. Kim, J. W. Cho, S. Woo, K. Park, and I. S. Kweon. Labor: Labeling only if required for domain adaptive semantic segmentation. In *Proceedings of the IEEE/CVF International Conference on Computer Vision*, pages 8588–8598, 2021.
- [45] I. Shin, S. Woo, F. Pan, and I. S. Kweon. Two-phase pseudo label densification for self-training based domain adaptation. In *Computer Vision–ECCV 2020: 16th European Conference, Glasgow, UK, August 23–28, 2020, Proceedings, Part XIII 16*, pages 532–548. Springer, 2020.
- [46] A. Singh. Clda: Contrastive learning for semi-supervised domain adaptation. In M. Ranzato, A. Beygelzimer, Y. Dauphin, P. Liang, and J. W. Vaughan, editors, *Advances in Neural Information Processing Systems*, volume 34, pages 5089–5101. Curran Associates, Inc., 2021.
- [47] A. Singh, N. Doraiswamy, S. Takamuku, M. Bhalerao, T. Dutta, S. Biswas, A. Chepuri, B. Vengatesan, and N. Natori. Improving semi-supervised domain adaptation using effective target selection and semantics. In *2021 IEEE/CVF Conference on Computer Vision and Pattern Recognition Workshops (CVPRW)*, pages 2703–2712, 2021.
- [48] S. Sinha, S. Ebrahimi, and T. Darrell. Variational adversarial active learning. In *Proceedings of the IEEE/CVF International Conference on Computer Vision*, pages 5972–5981, 2019.
- [49] J.-C. Su, Y.-H. Tsai, K. Sohn, B. Liu, S. Maji, and M. Chandraker. Active adversarial domain adaptation. In *Proceedings of the IEEE/CVF Winter Conference on Applications of Computer Vision*, pages 739–748, 2020.
- [50] D. Surís, R. Liu, and C. Vondrick. Learning the predictability of the future. In *Proceedings of the IEEE/CVF Conference on Computer Vision and Pattern Recognition*, pages 12607–12617, 2021.
- [51] A. Tifrea, G. Bécigneul, and O.-E. Ganea. Poincaré glove: Hyperbolic word embeddings. *arXiv preprint arXiv:1810.06546*, 2018.
- [52] M. van Spengler, E. Berkhout, and P. Mettes. Poincaré resnet, 2023.
- [53] T.-H. Vu, H. Jain, M. Bucher, M. Cord, and P. Perez. Advent: Adversarial entropy minimization for domain adaptation in semantic segmentation. In *Proceedings of the IEEE/CVF Conference on Computer Vision and Pattern Recognition (CVPR)*, June 2019.
- [54] D. Wang and Y. Shang. A new active labeling method for deep learning. In *2014 International joint conference on neural networks (IJCNN)*, pages 112–119. IEEE, 2014.
- [55] K. Wang, D. Zhang, Y. Li, R. Zhang, and L. Lin. Cost-effective active learning for deep image classification. *IEEE Transactions on Circuits and Systems for Video Technology*, 27(12):2591–2600, 2016.
- [56] T.-H. Wu, Y.-S. Liou, S.-J. Yuan, H.-Y. Lee, T.-I. Chen, K.-C. Huang, and W. H. Hsu. D 2 ada: Dynamic density-aware active domain adaptation for semantic segmentation. In *Computer Vision–ECCV 2022: 17th European Conference, Tel Aviv, Israel, October 23–27, 2022, Proceedings, Part XXIX*, pages 449–467. Springer, 2022.
- [57] T.-H. Wu, Y.-C. Liu, Y.-K. Huang, H.-Y. Lee, H.-T. Su, P.-C. Huang, and W. H. Hsu. Redal: Region-based and diversity-aware active learning for point cloud semantic segmentation. In *Proceedings of the IEEE/CVF International Conference on Computer Vision*, pages 15510–15519, 2021.
- [58] B. Xie, L. Yuan, S. Li, C. H. Liu, and X. Cheng. Towards fewer annotations: Active learning via region impurity and prediction uncertainty for domain adaptive semantic segmentation. In *Proceedings of the IEEE/CVF Conference on Computer Vision and Pattern Recognition (CVPR)*, pages 8068–8078, June 2022.
- [59] B. Xie, L. Yuan, S. Li, C. H. Liu, X. Cheng, and G. Wang. Active learning for domain adaptation: An energy-based approach. In *Proceedings of the AAAI Conference on Artificial Intelligence*, volume 36, pages 8708–8716, 2022.
- [60] Y. Yang and S. Soatto. Fda: Fourier domain adaptation for semantic segmentation. In *Proceedings of the IEEE/CVF Conference on Computer Vision and Pattern Recognition (CVPR)*, June 2020.
- [61] F. You, J. Li, L. Zhu, Z. Chen, and Z. Huang. Domain adaptive semantic segmentation without source data. In *Proceedings of the 29th ACM International Conference on Multimedia*, MM ’21, page 3293–3302, New York, NY, USA, 2021. Association for Computing Machinery.

- [62] P. Zhang, B. Zhang, T. Zhang, D. Chen, Y. Wang, and F. Wen. Prototypical pseudo label denoising and target structure learning for domain adaptive semantic segmentation. In *Proceedings of the IEEE/CVF conference on computer vision and pattern recognition*, pages 12414–12424, 2021.
- [63] Z. Zheng and Y. Yang. Rectifying pseudo label learning via uncertainty estimation for domain adaptive semantic segmentation. *International Journal of Computer Vision*, 129(4):1106–1120, 2021.
- [64] Y. Zou, Z. Yu, B. V. Kumar, and J. Wang. Unsupervised domain adaptation for semantic segmentation via class-balanced self-training. In *Proceedings of the European Conference on Computer Vision (ECCV)*, pages 289–305, 2018.
- [65] Y. Zou, Z. Yu, X. Liu, B. V. Kumar, and J. Wang. Confidence regularized self-training. In *The IEEE International Conference on Computer Vision (ICCV)*, October 2019.

Appendix

This appendix provides additional information and insights on the proposed Hyperbolic Active Learning Optimization (HALO) for semantic segmentation under domain shift.

This supplementary material is structured as follows:

- A.1: Additional Ablation Studies** presents additional ablation studies on the embedding dimensions and the proposed Hyperbolic Feature Reweighting (HFR) for Euclidean and hyperbolic backbones;
- A.2 Limitations** discusses current limitations and recommendations for further research;
- A.3 Broader Impact** regards future applications and the fostered progress in the field of Hyperbolic Neural Networks;
- A.4 Additional Hyperbolic Formulas** reports additional employed hyperbolic formulas;
- A.5 Qualitative Results** showcases representative qualitative results of HALO;
- A.6 Data Acquisition Strategy: class contour and within** discusses the data acquisition strategy with relation to pixels at the class contour or within that;
- A.7 Data Acquisition Strategy: rounds of selections** illustrates examples of pixel labeling selection and the priorities of the data acquisition strategy at each acquisition round.

A.1 Additional Ablation Studies

Embedding dimensions Table A1 compares the performance of Euclidean and hyperbolic models for different numbers of embedding dimensions (10, 64, and 512), for the source-only (pre-trained model) and source+target (active domain adapted – ADA) protocols. In line with the findings of [2], the source-only hyperbolic DeepLab-v3+ model demonstrates superior performance compared to the Euclidean counterpart, particularly for lower dimensions (10, 64).

In the source+target case of ADA, HALO demonstrates robustness across various embedding dimensions, achieving the highest performance with 64 channels (74.1% mIoU), but only slight decreases with 512 (73.7% mIoU) and 10 (73.8% mIoU). This suggests that a lower embedding dimension is sufficient and effective for representation learning.

Results of HFR Table A2 provides insights into the performance of hyperbolic and Euclidean models with and without Hyperbolic Feature Reweighting (HFR). In the case of HALO, the performance with and without HFR remains the same in the source-only setting. However, when applied to the source+target ADA scenario, HFR leads to an improvement of 1.2%. It should be noted that HFR also stabilizes the training of hyperbolic models. In fact, when not using HFR, training requires a warm-up schedule and, still, it does not converge in approximately 20% of the runs. HFR improves therefore performance for ADA and it is important for hyperbolic learning stability.

Table A1: Performance comparison of Euclidean and hyperbolic models with varying output channels (10, 64, and 512) in source-only and source+target protocols.

| Encoder | Protocol | Channels | mIoU (%) |
|-------------------|----------------------|-----------|-------------|
| DeepLab-v3+ | source-only | 10 | 37.3 |
| DeepLab-v3+ | source-only | 64 | 37.9 |
| DeepLab-v3+ | source-only | 512 | 36.3 |
| Hyper DeepLab-v3+ | source-only | 10 | 39.7 |
| Hyper DeepLab-v3+ | source-only | 64 | 38.9 |
| Hyper DeepLab-v3+ | source-only | 512 | 35.9 |
| RIPU [58] | source+target | 10 | 72.3 |
| RIPU [58] | source+target | 64 | 72.0 |
| RIPU [58] | source+target | 512 | 71.2 |
| HALO | source+target | 10 | 73.8 |
| HALO | source+target | 64 | 74.1 |
| HALO | source+target | 512 | 73.7 |

Table A2: **HFR Performance Comparison:** Evaluating the impact of Hyperbolic Feature Reweighting (HFR) on hyperbolic and Euclidean models in source-only and source+target protocols.

| Encoder | Protocol | HFR | mIoU (%) |
|-------------------|----------------------|-----|-------------|
| DeepLab-v3+ | source-only | ✗ | 36.3 |
| DeepLab-v3+ | source-only | ✓ | 22.7 |
| Hyper DeepLab-v3+ | source-only | ✗ | 39.0 |
| Hyper DeepLab-v3+ | source-only | ✓ | 38.9 |
| HALO | source+target | ✗ | 72.9 |
| HALO | source+target | ✓ | 74.1 |

A.2 Limitations

We have presented experimental evidence that a novel interpretation for the hyperbolic radius is needed, since neither the hierarchical nor the uncertainty-based explain our findings. We have also employed the proposed interpretation for a new model and data acquisition strategy, which yields state-of-the-art performance. Future research should reconsider the evidence and our empirical analysis from a mathematical perspective, proving the properties of the hyperbolic radius in the given experimental setup, which we have not covered in this work. Future research should also re-conduct the three interpretations to a unified formal framework, from which these may be derived.

The work has shown that Active Learning and Domain Adaptation reduce labelling efforts and yield performance beyond the fully-supervised trained models. This setup remains limited to having a source model, pre-trained on a large labelled dataset. In the case of HALO, the source model leverages synthetic data. It needs therefore large simulation efforts, and it requires the downstream synthetic-to-real adaptation. Pre-training on a real source dataset self-supervisedly seems a promising research direction, which we have not discussed here, to alleviate simulation efforts and reduce the domain shift.

A.3 Broader Impact

Hyperbolic Neural Networks (HNN) have recently become mainstream, reaching state-of-the-art across several tasks. Still, the theory and interpretation of HNN is diverse across tasks. Specifically, the hyperbolic radius has been interpreted as a continuum hierarchical parent-to-child measure or as an estimate of uncertainty. Our novel third way of interpreting the radius adds to the flourishing framework of HNN, making a step forward.

Our research presents an effective approach for pixelwise annotation that offers cost savings and surpasses the performance of fully supervised learning. As the demand for additional data increases,

practical methods such as active domain adaptation are expected to play a prominent role in new dataset creation and model training. HALO has the potential to contribute to advancements in various fields, including self-driving cars, manufacturing, and medicine. However, it is crucial to acknowledge that since the model learns from human annotators, it can introduce biases and errors in its predictions. Active domain adaptation adds complexity due to a reduced number of labels but enhances the interpretability of the model’s learning process. It is important, as with any new technology, to implement safety measures to prevent misuse and ensure the verification of inputs.

A.4 Additional Hyperbolic Formulas

Here we report established hyperbolic formulas which have used in the paper, but not shown due to space constraints.

Poincaré Distance Given two hyperbolic vectors $x, y \in \mathbb{D}_c^N$, the *Poincaré distance* represents the distance between them in the Poincaré ball and is defined as:

$$d_{Poin}(x, y) = \frac{2}{\sqrt{c}} \tanh^{-1}(\sqrt{c} \| -x \oplus_c y \|) \quad (A1)$$

where \oplus_c is the Möbius addition defined in Eq. 2 of the paper and c is the manifold curvature.

Riemannian Variance Given a set of hyperbolic vectors $x_1, \dots, x_M \in \mathbb{D}_c^N$ we define the Riemannian variance between them as:

$$\sigma^2 = \frac{1}{M} \sum_{i=1}^M d_{Poin}^2(x_i, \mu) \quad (A2)$$

where μ is the Fréchet mean, the hyperbolic vector that minimizes the Riemannian variance. μ cannot be computed in closed form, but it may be approximated with a recursive algorithm [27].

A.5 Qualitative Results

In this section, we present visualizations of the predicted segmentation maps, acquisition function outputs, and pixel selections of HALO, and compare them with RIPU to assess the improvements achieved. Notably, HALO outperforms RIPU in challenging class separations. The clear separation between the *driver* and *bike* classes is evident in Fig. 9a and 9c, as well as in Fig. 10c. HALO also demonstrates superior segmentation performance for classes such as *poles* and *signs*, as observed in Fig. 9c and 9d, and Fig. 10b and 10d. Furthermore, notable improvements are seen in segmenting the *wall* class (Fig. 9b and 10a), as well as the *truck* class (Fig. 9b).

Let us now examine the observed limitations in RIPU’s data acquisition strategy for budgets exceeding 2%. This issue becomes apparent in the RIPU pixel selections depicted in Figs. 9 and 10. Due to RIPU’s heavy pruning of pixels in regions distant from class contours, the selection process exhausts the available pixels and starts sampling them regularly from the left-most part of the image. The observed data acquisition strategy in RIPU does not significantly impact its performance, as supplementing the selected pixels with regularly-sampled ones still benefits model training. In contrast, HALO’s hyperbolic boundaries offer a broader selection of pixels, and larger budgets adhere to HALO’s proposed data acquisition strategy, resulting in improved performance.

A.6 Data Acquisition Strategy: class contour and within

By means of the proposed hyperbolic boundaries, HALO considers informative pixels at the contour of classes but also within the areas, and at the object-object interface. In this section, we analyze quantitatively and qualitatively the statistics from these two categories of selected pixels, i.e. *class contours* and *within*. Here we take as contours those regions of size 15×15 , centered on the ground-truth class contours. We deem this a thick contour, well representative for statistics of contour/within selected pixel numbers. We flag all other pixels outside the thick contour as *within*.

Consider the cityscape validation set, the average percentage of contour pixels is 51.63% while the internal ones are 48.37%. The two percentages are close, which remarks how HALO leverages the intra-class details considerably to improve classification prediction.

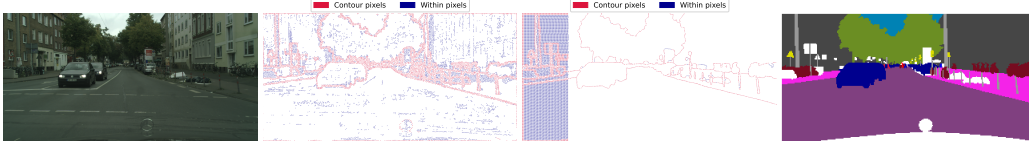


Figure 6: a) Original image. b) Selected pixels after 5% HALO acquisition rounds. In red, the pixels on the contours between different classes, and in blue, the pixels within each class. c) Selected pixels after 5% RIPU acquisition rounds. d) GT labels.

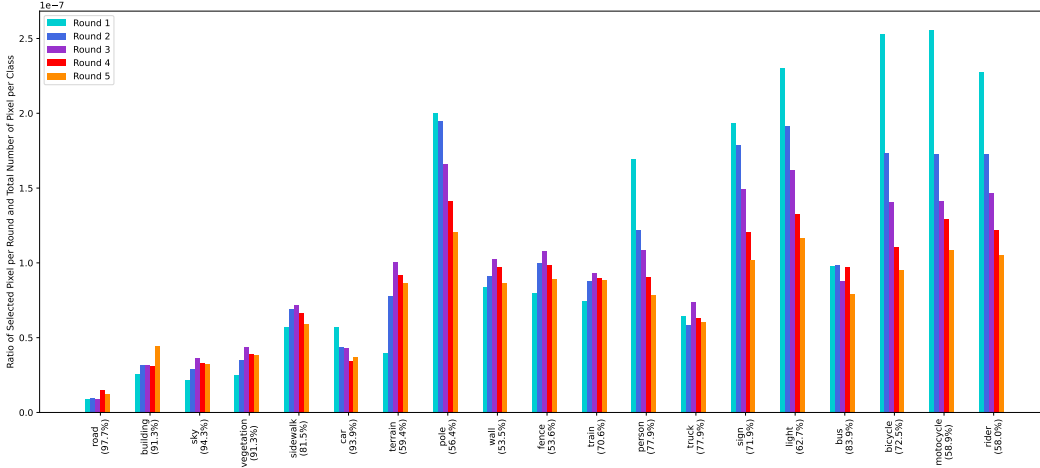


Figure 7: Ratio between the selected pixels for each class at each round and the total number of pixels per class. Each color shows the ratio in the specific round. On the x -axis are reported the classes with the relative mIoU (%) of HALO (cf. Table 1 of the main paper) ordered according to they decreasing hyperbolic radius.

In Fig. 6b, we report an example of the pixels selected with HALO distinguishing the selection on the class contours (red) and within (blue). The statistics for this sample are 52.56% for the contours and 47.44% for pixels within, which are in line with the statistics on the whole dataset.

In Fig. 6c, we have the selection done using RIPU. As discussed in Sec. A.5, when the budget is too high, RIPU’s acquisition strategy fails, selecting uniformly pixels from the left-most image part when the contour pixels are over. In the considered example, the statistics for the pixels sampled with RIPU’s strategy are 90.02% for the contours and 9.98% for pixels within classes.

Comparing our selection (Fig. 6b) with the ground truth labels (Fig. 6d), we observe how our model correctly detects the contours between the classes (e.g., car, bicycles, poles) using the hyperbolic radius exclusively. Referring to the original image (Fig. 6a), we can notice the intra-class elements. Here the model focuses on the details of the right-side building (e.g., windows and doors) but also of the road (e.g., road markings). The model also acquires pixels within the more difficult classes, e.g., the inside of the pole on the right side or the inside part of traffic signs. This remarks how the model prioritizes the selection for the classes that it considers more difficult, not only at the class contours, thanks to leveraging hyperbolic boundaries based on the hyperbolic radius variations.

A.7 Data Acquisition Strategy: rounds of selections

In this section, we analyze how the model prioritizes the selection of the pixels during the different rounds. In Fig. 7, we consider the ratio between the selected pixel at each round and the total number of pixels for the considered class. Note how the model selects in the early stages from the class with high intrinsic difficulty (e.g., rider, bicycle, pole). During the different rounds, the selected pixels decrease because of the scarcity of pixels associated with these classes. On the other hand, the classes with lower intrinsic difficulty are less considered in the early stages and the model selects from them

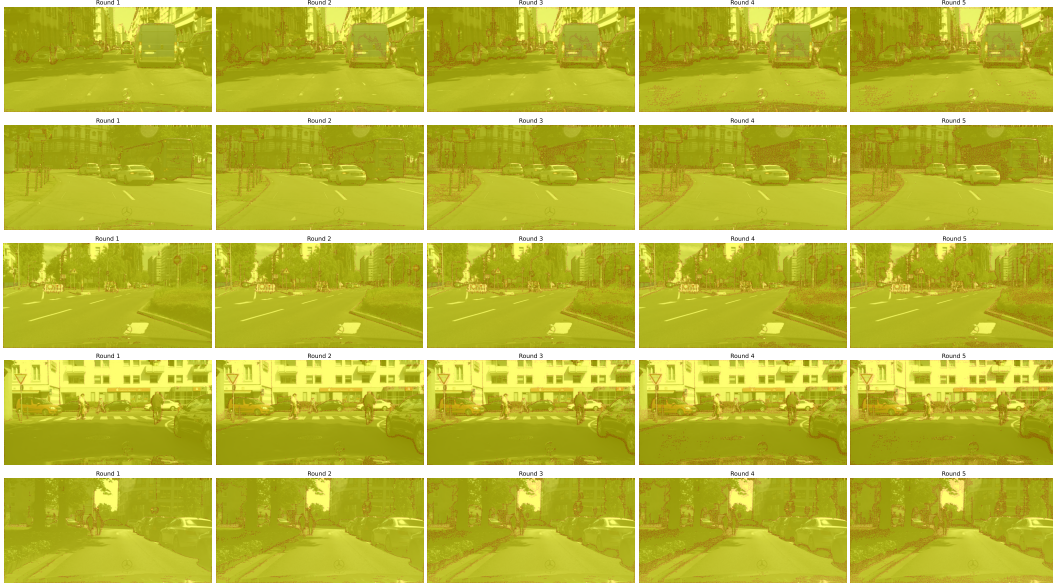
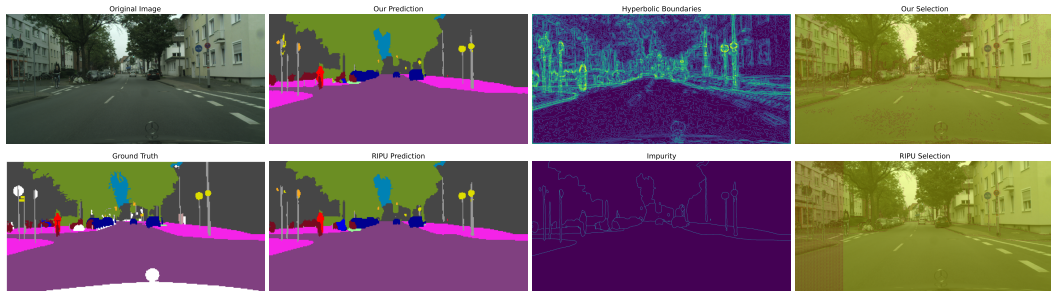


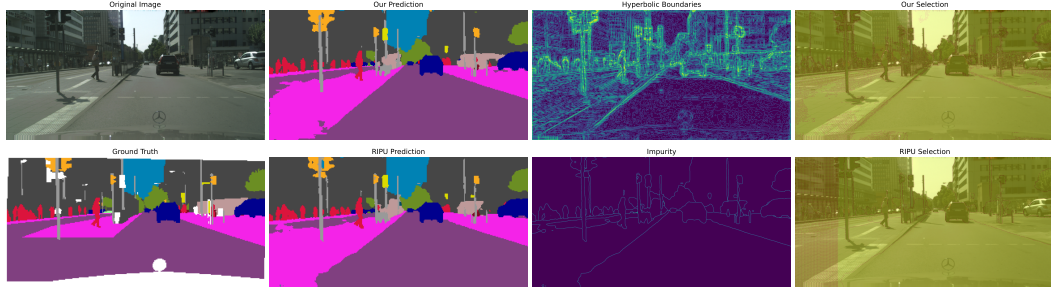
Figure 8: Qualitative analysis on the pixel selected by HALO at each round.

in the intermediate rounds if the class has an intermediate inherent complexity (e.g., wall, fence, sidewalk) or in the last stages if the classes are easiest (e.g., road or building).

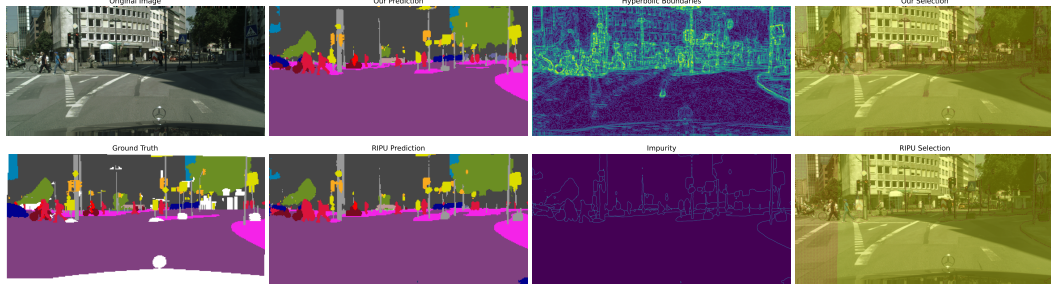
The qualitative samples of pixel selections in Fig. 8 also support this statement. In the first rounds (left-most column), HALO prioritizes the pixels on the contour of the classes with high intrinsic variability (e.g. rider, person, poles, signs). In the second round, it continues detecting contours from challenging classes but it starts considering also contours from other ones (e.g. car, road). In the final rounds (right-most columns), HALO selects from contours but it also considers within details, which benefits the model learning of intra-class variability. Consider as examples the internal part of the bus in the second row; or details from the building (e.g., windows) and the road (e.g., the manhole) in the fourth row. We summarize that the model prioritizes the contours, selected from more to less complex classes throughout the stages. However, the model also considers details from within classes and objects as informative details, especially at later data acquisition stages.



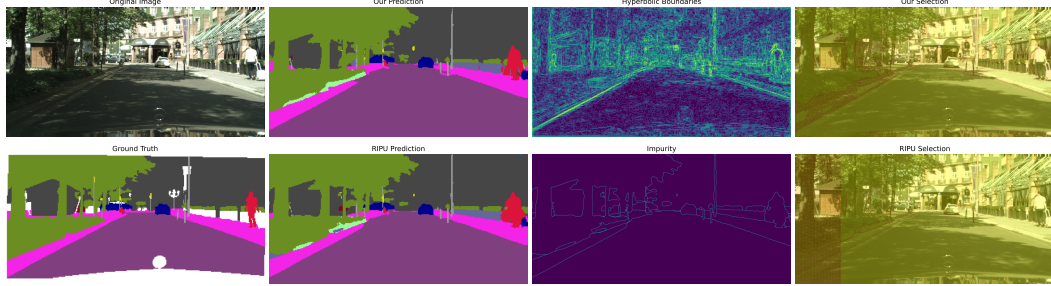
(a)



(b)



(c)



(d)

Figure 9: **Segmentation Results Visualization for the GTAV → Cityscapes Task.** The figure showcases different subfigures representing the original image, HALO’s prediction, Hyperbolic Boundaries output, and HALO’s pixel selection in the first row. The second row displays the ground-truth label, RIPU’s prediction, Region Impurity output, and RIPU’s pixel selection.

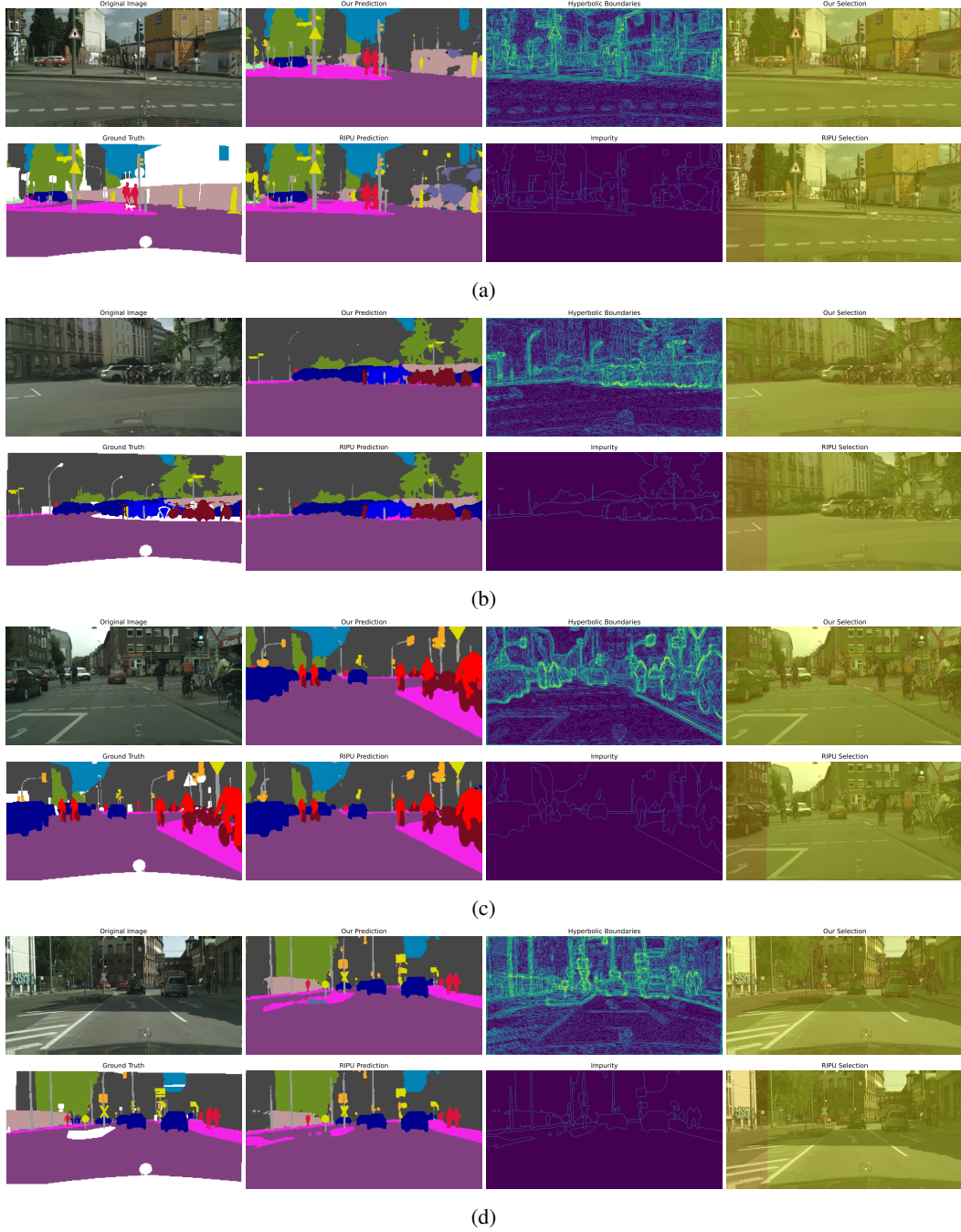


Figure 10: **Segmentation Results Visualization for the GTAV → Cityscapes Task.** This figure follows the same structure as Fig. 9.